Supplement of Atmos. Chem. Phys., 21, 16745–16773, 2021
https://doi.org/10.5194/acp-21-16745-2021-supplement

Supplement of

Measurement report: Comparison of airborne, in situ measured, lidar-based, and modeled aerosol optical properties in the central European background – identifying sources of deviations

Sebastian Düsing et al.

Correspondence to: Sebastian Düsing (duesing@tropos.de)

Supplementary text

This supplementary text provides deeper insights on the methodology and measurements described in the manuscript "Measurement report: Comparison of airborne in situ measured, lidar-based, and modeled aerosol optical properties in the Central European background – identifying sources of deviations".

Measurement strategy with the airborne cloud and turbulence observation system (ACTOS)

A typical flight pattern for one of the conducted measurement flights is displayed exemplarily for 28 June 2015, in Fig. S1 as a red line. Typically, a measurement flight lasted around two hours and started with a profile to characterize the atmosphere vertically up to altitudes of 2700 m and to identify atmospheric layers of interest. Afterward, sections of constant flight height, so-called "legs" were flown with at least 10 minutes duration to realize measurements within on altitude level and to increase the counting statistics for other measurements, such as the PNSD with a lower time resolution and such as the aerosol particle absorption coefficient deployed on ACTOS. Figure S1 also displays color-coded the attenuated $\sigma_{\mathrm{bsc}}(\lambda)$ at 1064 nm in Mm^{-1} sr^{-1} measured by Polly$^{\mathrm{XT}}$ lidar on 28 June 2015, between 06:00 UTC and noon. Bright white color represents a strong backscatter signal and indicates clouds. The development of the planetary boundary layer is visible with the increasing cloud bottom height of 500 m at 06:00 UTC and around 1600 m altitude at noon. Also, the residual layer containing some aerosol layer aloft the top of the planetary boundary layer (PBL) between 1250 m and 2300 m is visibly indicated by greenish colors. Therefore, the payload was sampling in the free troposphere and within the planetary boundary layer and was sampling different aerosol populations. A short period at around 09:30 UTC of low-level clouds interfered with the lidar measurements during the flight.

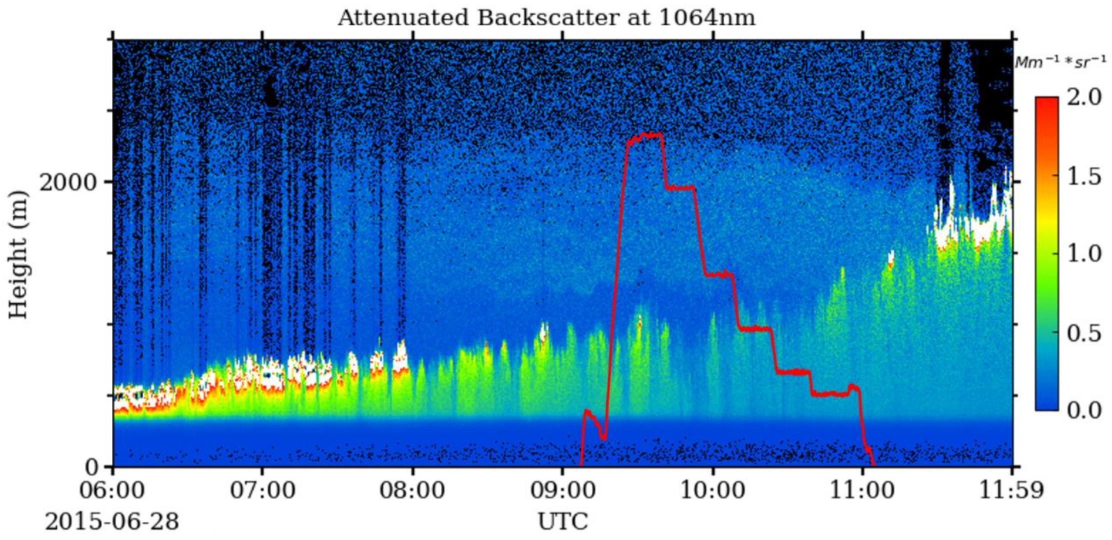

Figure S1. Attenuated aerosol particle light backscatter coefficient ($\sigma_{\mathrm{bsc}}(\lambda)$, color-coded) measured with Polly$^{\mathrm{XT}}$ lidar at 1064 nm on 28 June 2015, between 6:00 UTC and 12:00 UTC is displayed. White colors indicate values larger than 2.0 Mm^{-1} sr^{-1}. The red line represents the flight pattern of ACTOS in terms of altitude in m above ground.

Experiments in the context of aerosol load and air mass

In the following, both campaigns' measurement days of interest will be set in context to aerosol load and air mass origin of the shown period. Each day in both campaigns was assigned to its corresponding air-mass back-trajectory from a pool of in total 15 clusters following Sun et al. (2020). These clusters are appointed by the season (cold season, CS; transition season, TS; and warm season, WS) and the prevalent synoptic pattern. The abbreviation ST indicates a stagnant pattern; A indicates anticyclonic patterns with air masses originating in eastern (1) and western (2) Europe. C represents a cyclonic pattern with air masses originating from the south (1) and north (2). The prevalent trajectory cluster is assigned with red or blue colors indicating polluted or clean conditions and the respective key. Clusters with keys CS-ST, CS-A1, CS-A2, CS-C1, TS-A1, WS-ST, WS-A1, and WS-C1 represent polluted conditions. Briefly, the clustering is based on a k-means clustering method for meteorological back-trajectories (Dorlin et al., 1992). Further details are present by Ma et al. (2014) and the supplementary material of Sun et al. (2020).

During the summer campaign, 14 flights were conducted, two of which were test flights. Low-level clouds strongly attenuate the lidar measurements. Therefore, after screening the weather conditions of all conducted flights for periods of low-level cloud coverage, four measurement flights performed on three days have been left for further investigation with preferable mostly clear sky conditions. The gray shaded boxes in Fig. S2 mark the three investigated days without low-level clouds of this study.

Figure S2a shows the time series of equivalent black carbon mass concentration (m_{eBC}) at Melpitz Observatory during June 2015, derived with daily (midnight to midnight) filter-measurement-based mass absorption cross-sections estimates at 637 nm (*MAC*(637 nm)). Figure S2b displays the time series of the number concentration of all aerosol particles up to a size of 800 nm in diameter. The $\sigma_{\mathrm{sca}}(\lambda)$ and $\sigma_{\mathrm{abs}}(\lambda)$ at 450, 550, and 700 nm, and 637 nm, respectively, are shown Fig. S2c**.**

During this period, the average m_{eBC} was 0.23 (± 0.14) µg m^{-3} (range from 0.04 to 1.2 µg m^{-3}), which is in the range of the median m_{eBC} for cleaner air-masses (cluster keys: CS-C2a, CS-C2b, TS-A2, TS-C1, TS-C2, WS-A2, and WAS-C2) as reported by Sun et al. (2020).

The three investigated days cover a wide range of the observed m_{eBC} (0.03 to 0.58 µg m^{-3}) during the intensive period between 15 June and 28 June 2015. Daily mean m_{eBC} of 0.14 (± 0.05) µg m^{-3} were observed during 17 June, 0.35 (± 0.05) µg m^{-3} during 26 June, and 0.095 (± 0.03) µg m^{-3} during 28 June 2015. The three days are characterized by westerly inflows (trajectory cluster WS), and the air mass originated from the North Atlantic (WS-A2 (clean); 17 June and 26 June and WS-C2 (clean); 28 June; Sun et al., 2020). Flight 20150617b was conducted at relatively clean conditions, whereas flight 20150626a was conducted within a period of comparatively high m_{eBC}.

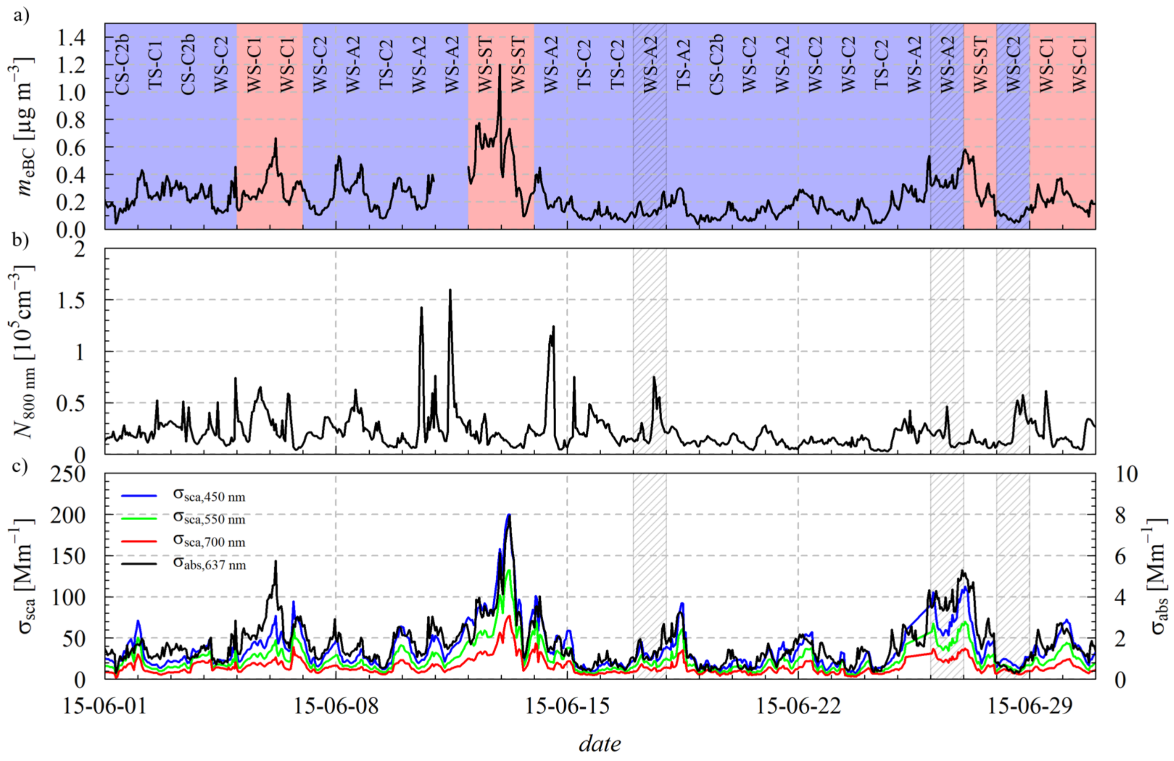

Figure S2. Panel **a)** depicts equivalent black carbon mass concentration (m_{eBC}) from 1 June to 30 June 2015. Color codes represent clean (blue) and polluted (red) trajectory clusters with the given keys for each day following the trajectory clustering presented by Sun et al. (2020). Clustering is explained below. Panel **b)** shows the total number concentration of all aerosol particles between 5 and 800 nm in diameter ($N_{800\mathrm{nm}}$) and **c)** displays the aerosol particle light scattering (σ_{sca}) and absorption coefficient (σ_{abs}). Grey shaded areas show the measurement days investigated in more detail.

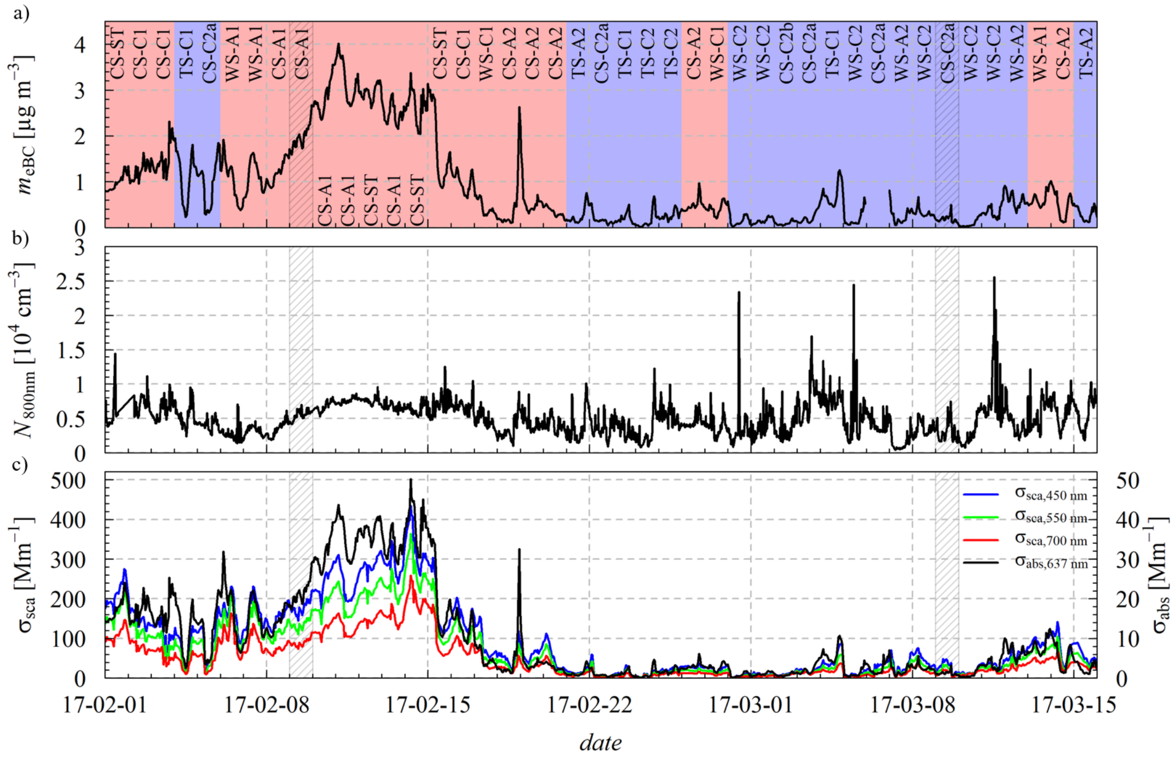

Figure S3. Same as Fig. S2, for the period 1 February to 15 March 2017.

Two cases from 9 February and 9 March 2017 are used for the data analysis in the winter campaign. The aerosol conditions and air mass origins from 1 February to 16 March are displayed in Fig. S3. The presented cases are representatives of two distinct periods within this time frame. Period 1 from 1 February to about 19 February is featured by a high m_{eBC} of up to 4.0 µg m^{-3}, while the subsequent period is relatively clean. This maximum m_{eBC} was in the same range as the observed maximum refractory black carbon (rBC) mass concentration (m_{rBC}) of 4 µg m^{-3} reported by Yuan et al. (2020) at Melpitz between 1 February and 19 February 2017. Long-term measurements at Melpitz from 2009-2014 reported by Birmili et al. (2016) were characterized by an average m_{eBC} of 0.9 µg m^{-3}. Trajectory clusters CS-A1 and CS-ST, categorized as polluted, are assigned from 8 February to 15 February. In this period, the air masses were transported from northern Ukraine crossing southern Poland (cluster CS-A1; Sun et al., 2020), a hotspot of elemental carbon emissions (see 7x7 km-EUCAARI EC-emissions in Chen et al., 2016). The combination of air mass origins (East Europe and stationary) resulted in an accumulation of pollution over Melpitz. The mass concentration of aerosol particles with an aerodynamic diameter lower than 2.5 µm ($PM_{2.5}$) on 9 February exceeds typical annual average $PM_{2.5}$ aerosol particle mass concentrations (e.g., Spindler et al., 2013; 20.1 ± 18 µg m^{-3}) by a factor of two and illustrates the unusually high pollution during this period.

Quality of used Mie-Model

For the investigations within the manuscript, a Mie-model is utilized. The underlying assumptions within the Mie-Model are validated using a correlation of the measured and Mie-based aerosol optical properties in the dried state (see Fig. S4) and with the in-situ measured σ_{ext}(630 nm) derived on ACTOS (see Fig. S5).

Considering the correlation with the ground-based in-situ measurements of σ_{sca}(450 nm), the result of the Mie-model agrees within 3 % during the summer campaign (underestimation; see Fig. S4a) and within 13 % (overestimation; Fig. S4b) during the winter period. Based on the correlation in Fig. S4, the Mie-model reproduces the $\sigma_{abs}(\lambda)$ derived with the MAAP at 637 nm within 8 % (Fig. S4b) during winter, and within 18 % (Fig. S4a) during the summer period overestimating the measured $\sigma_{abs}(\lambda)$ in both cases.

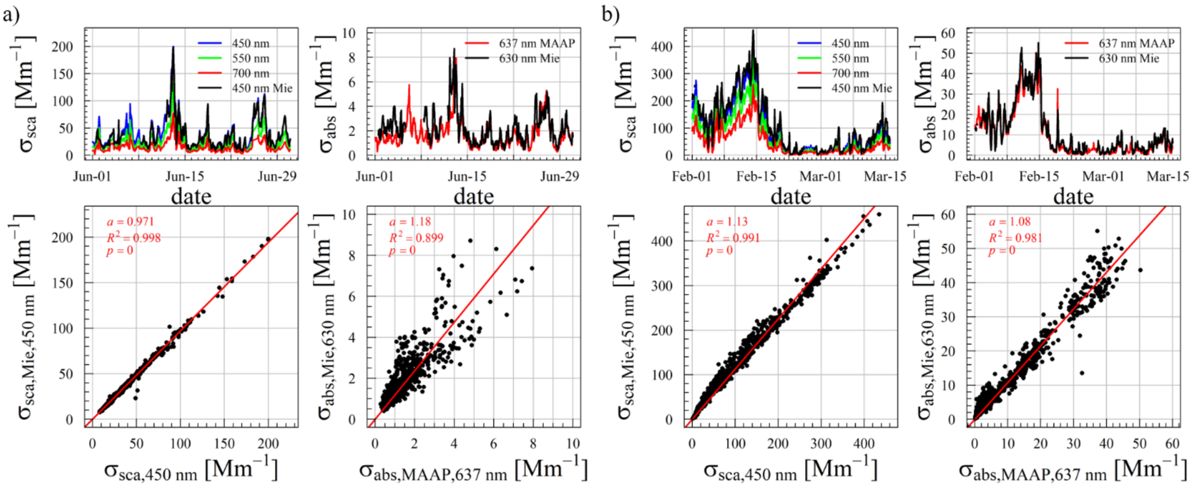

Figure S4. Time series (upper panels) and scatter plot (lower panels) of modeled and measured aerosol particle light scattering ($\sigma_{sca}(\lambda)$, left panels) and absorption ($\sigma_{abs}(\lambda)$, right panels) coefficients derived with the Mie-model and the Nephelometer and MAAP for different wavelength (color-coded) at Melpitz Observatory during the summer **(a)** and winter campaign **(b).**

In the summer case, two distinct clusters in the $\sigma_{abs}(\lambda)$, one above and one below the fitting line, indicate different aerosol types and that the model constraints might better represent the prevalent aerosol type of lower cluster better since the data points are close to the 1:1 line. The aerosol represented by the lower cluster was prevalent at Melpitz from 13 June 2015 on, and the comparison of the modeled and measured $\sigma_{ext}(\lambda)$ ($\sigma_{sca}(\lambda)$) shows an agreement within 4 % (2 %). Therefore, the mixing approach within the model is a good representation of the aerosol present during the intensive period of the measurement campaign in the summer between 15 June and 28 June 2015.

However, the model utilized rough assumptions to represent the aerosol. Besides the assumption of a wavelength-independent complex aerosol refractive index, the assumption of a constant volume fraction of eBC underestimates the BC content in the smaller aerosol particles. It leads to an overestimation in the larger aerosol particles because BC usually is primarily found in the aerosol accumulation and Aitken mode (Bond et al., 2013) with a mass peak at around 250 nm of BC core diameter. Also, the coating thickness of same-sized soot cores is not constant, and the size of BC cores covers only a specific size range, as shown by Ditas et al. (2018). During the summer campaign, no size-resolved BC mass concentration measurements have been available and would also be limited to a specific size range. Therefore, implementing a constant eBC volume fraction within an optical model is a handy approach and is often used in other studies (e.g., Düsing et al., 2018; Ma et al., 2014, 2012).

Furthermore, the model validation in terms of absorption is based on the MAC(637 nm) estimates based on the MAAP measurements and hence most representative at this wavelength. Modeled $\sigma_{abs}(\lambda)$ at lower or larger wavelengths could deviate from measurements because of a different value of MAC(λ).

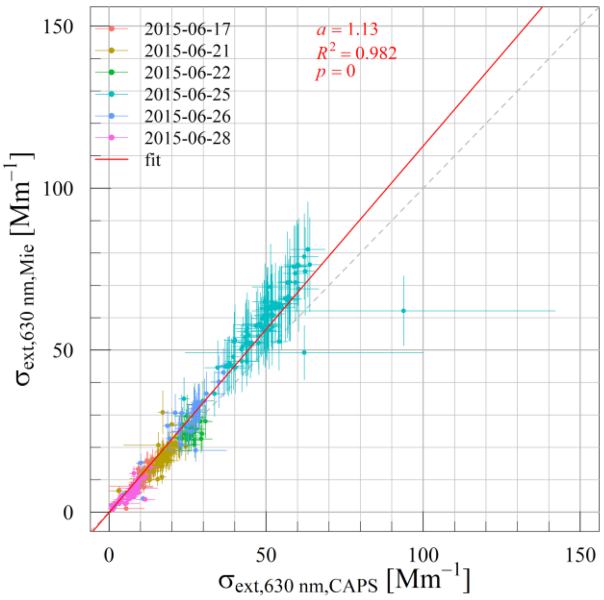

Figure S5. Scatter plot of the in-situ airborne measurement-based aerosol particle light extinction coefficient (σ_{ext}) derived with the CAPS and the Mie model at 630 nm in the dried state. The red line indicates the linear fit of both, the gray dashed line represents the 1:1 line, and color-coded are the measurement days of the summer campaign.

However, considering the airborne in-situ correlation, the model agrees to measured σ_{ext}(630 nm) within 13 % (slope = 1.13 with $R^2 = 0.98$; $p = 0$) averaged over all available data points. Nevertheless, the modeled σ_{ext}(630 nm) overestimates the measured one, especially on 25 June (light blue data points). Excluding that day from the correlation, the model would overestimate the measured σ_{ext}(630 nm) by 2.2 % ($R^2 = 0.98$), which is within the measurement uncertainty of the CAPS. Note that for the airborne in-situ correlation, the underlying airborne PNSD used in the Mie-model is not corrected for diffusional and aspirational loss because both systems were sampling through the same inlet system. In winter, the altitude corrected PNSD measured at the ground, which is used to replace the missing aerosol particle size range (up to 300 nm), was corrected for the diffusional losses inside the tubing. Diffusional losses inside the tubing of the balloon platform lower the in-situ measured $\sigma_{abs}(\lambda)$. Therefore, the in-situ measured $\sigma_{abs}(\lambda)$ would have been smaller than modeled ones by default. To which extent, however, remains unclear.

Comparison of the hygroscopicity during summer campaign with ZSR-mixing approach

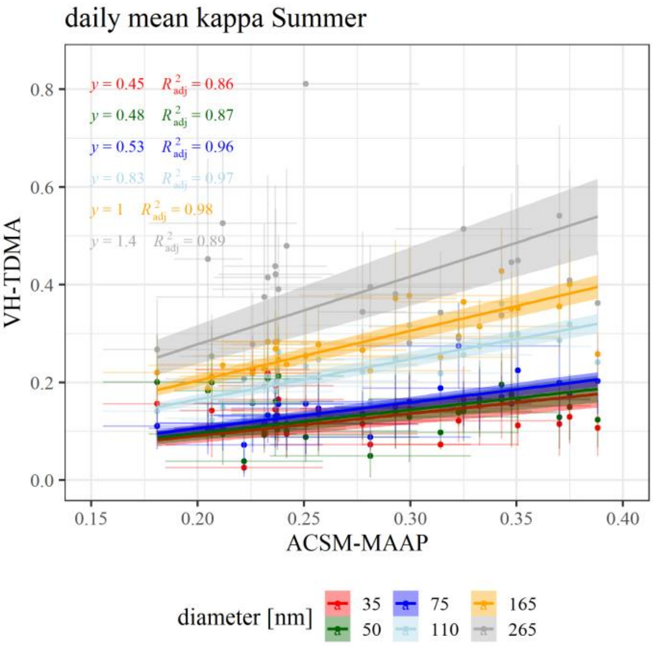

Figure S6. Scatter plot of the aerosol hygroscopicity derived with VH-TDMA (y-axis) and the ZSR-mixing approach combining ACSM and MAAP measurements (x-axis). Colors represent the size-bins of the VH-TDMA. Lines with shaded areas represent a linear fit and the uncertainty of fit. Fitting parameters are displayed with corresponding colors.

LR at dry state vs. ambient state

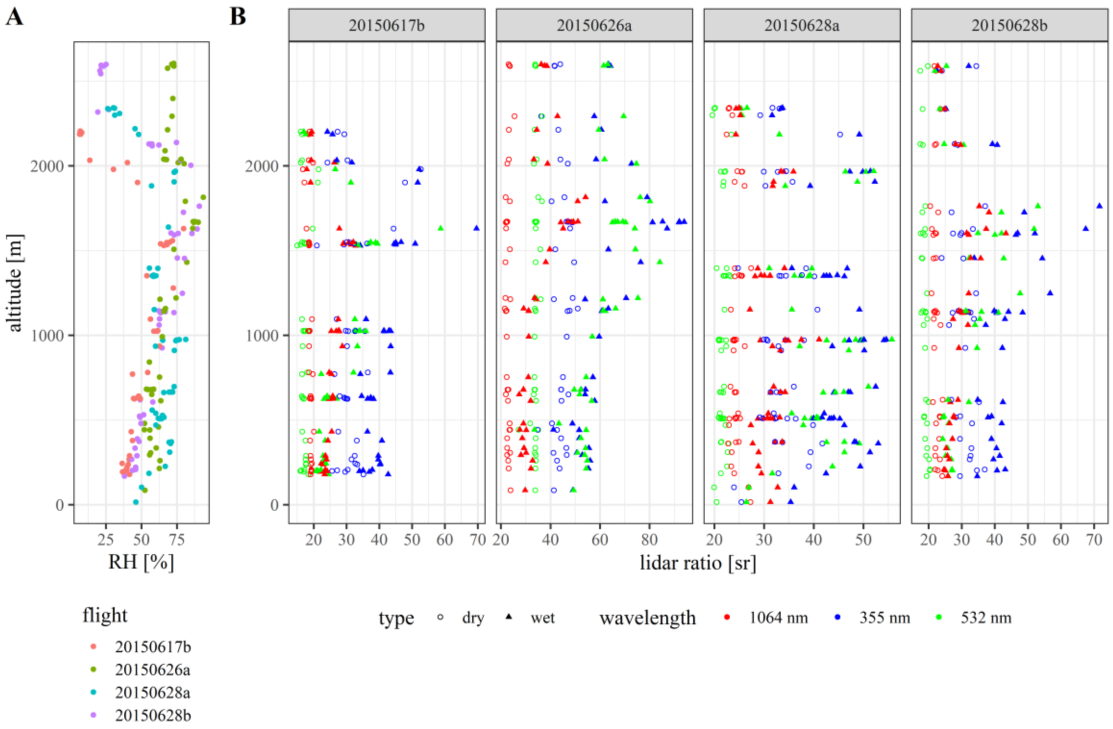

Figure S7. Profile of RH **(A)** and lidar ratio **(B)** modeled in dry (circles) and ambient state (triangles) for the four investigated flights of the study.

Figure S7A displays the profile of RH measured during the four flights of interest of the summer campaign. Figure S7B shows the profiles of the LR at 355, 532, and 1064 nm calculated with the Mie model in ambient (triangles) and dry (circles) state. While the LR changes only slightly, if at all, in the dry state, compared to the ambient state in which the change is more pronounced. Hence a direct relationship between LR and RH is visible.

References

Birmili, W., Weinhold, K., Rasch, F., Sonntag, A., Sun, J., Merkel, M., Wiedensohler, A., Bastian, S., Schladitz, A., Löschau, G., Cyrys, J., Pitz, M., Gu, J., Kusch, T., Flentje, H., Quass, U., Kaminski, H., Kuhlbusch, T. A. J., Meinhardt, F., Schwerin, A., Bath, O., Ries, L., Gerwig, H., Wirtz, K., and Fiebig, M.: Long-term observations of tropospheric particle number size distributions and equivalent black carbon mass concentrations in the German Ultrafine Aerosol Network (GUAN), Earth System Science Data, 8, 355–382, https://doi.org/10.5194/essd-8-355-2016, 2016.

Bond, T. C., Doherty, S. J., Fahey, D. W., Forster, P. M., Berntsen, T., DeAngelo, B. J., Flanner, M. G., Ghan, S., Kärcher, B., Koch, D., Kinne, S., Kondo, Y., Quinn, P. K., Sarofim, M. C., Schultz, M. G., Schulz, M., Venkataraman, C., Zhang, H. , Zhang, S., Bellouin, N., Guttikunda, S. K., Hopke, P. K., Jacobson, M. Z., Kaiser, J. W., Klimont, Z., Lohmann, U., Schwarz, J. P., Shindell, D., Storelvmo, T., Warren, S. G., and Zender, C. S.: Bounding the role of black carbon in the climate system: A scientific assessment, J. Geophys. Res. Atmos., 118, 5380–5552, https://doi.org/10.1002/jgrd.50171, 2013.

Chen, Y., Cheng, Y.-F., Nordmann, S., Birmili, W., Denier van der Gon, H. A. C., Ma, N., Wolke, R., Wehner, B., Sun, J., Spindler, G., Mu, Q., Pöschl, U., Su, H., and Wiedensohler, A.: Evaluation of the size segregation of elemental carbon (EC) emission in Europe: influence on the simulation of EC long-range transportation, Atmos. Chem. Phys., 16, 1823-1835, https://doi.org/10.5194/acp-16-1823-2016, 2016.

Ditas, J., Ma, N., Zhang, Y., Assmann, D., Neumaier, M., Riede, H., Karu, E., Williams, J., Scharffe, D., Wang, Q., Saturno, J., Schwarz, J., Katich, J., McMeeking, G., Zahn, A., Hermann, M., Brenninkmeijer, C., Andreae, M., Pöschl, U., Su, H., and Cheng, Y.: Strong impact of wildfires on the abundance and aging of black carbon in the lowermost stratosphere, Proceedings of the National Academy of Sciences, 115(50), E11595-E11603, https://doi.org/10.1073/pnas.1806868115, 2018.

Dorling, S. R., Davies, T. D., and Pierce, C. E.: Cluster analysis: A technique for estimating the synoptic meteorological controls on air and precipitation chemistry—Method and applications, Atmos. Environ., 26, 2575, https://doi.org/10.1016/0960-1686(92)90110-7, 1992.

Düsing, S., Wehner, B., Seifert, P., Ansmann, A., Baars, H., Ditas, F., Henning, S., Ma, N., Poulain, L., Siebert, H., Wiedensohler, A., and Macke, A.: Helicopter-borne observations of the continental background aerosol in combination with remote sensing and ground-based measurements, Atmos. Chem. Phys., 18, 1263–1290, https://doi.org/10.5194/acp-18-1263-2018, 2018.

Ma, N., Zhao, C. S., Müller, T., Cheng, Y. F., Liu, P. F., Deng, Z. Z., Xu, W. Y., Ran, L., Nekat, B., van Pinxteren, D., Gnauk, T., Müller, K., Herrmann, H., Yan, P., Zhou, X. J., and Wiedensohler, A.: A new method to determine the mixing state of light absorbing carbonaceous using the measured aerosol optical properties and number size distributions, Atmos. Chem. Phys., 12, 2381–2397, https://doi.org/10.5194/acp-12-2381-2012, 2012.

Ma, N., Birmili, W., Müller, T., Tuch, T., Cheng, Y. F., Xu, W. Y., Zhao, C. S., and Wiedensohler, A.: Tropospheric aerosol scattering and absorption over central Europe: a closure study for the dry particle state, Atmos. Chem. Phys., 14, 6241–6259, https://doi.org/10.5194/acp-14-6241-2014, 2014.

Spindler, G., Grüner, A., Müller, K., Schlimper, S., and Herrmann, H.: Long-term size-segregated particle (PM10, PM2.5, PM1) characterization study at Melpitz – influence of air mass inflow, weather conditions and season, J. Atmos. Chem., 70, 165–195, https://doi.org/10.1007/s10874-013-9263-8, 2013.

Sun, J., Birmili, W., Hermann, M., Tuch, T., Weinhold, K., Merkel, M., Rasch, F., Müller, T., Schladitz, A., Bastian, S., Löschau, G., Cyrys, J., Gu, J., Flentje, H., Briel, B., Asbach, C., Kaminski, H., Ries, L., Sohmer, R., Gerwig, H., Wirtz, K., Meinhardt, F., Schwerin, A., Bath, O., Ma, N., and Wiedensohler, A.: Decreasing trends of particle number and black carbon mass concentrations at 16 observational sites in Germany from 2009 to 2018, Atmos. Chem. Phys., 20, 7049–7068, https://doi.org/10.5194/acp-20-7049-2020, 2020.

Yuan, J., Modini, R. L., Zanatta, M., Herber, A. B., Müller, T., Wehner, B., Poulain, L., Tuch, T., Baltensperger, U., and Gysel-Beer, M.: Variability in the mass absorption cross section of black carbon (BC) aerosols is driven by BC internal mixing state at a central European background site (Melpitz, Germany) in winter, Atmos. Chem. Phys., 21, 635–655, https://doi.org/10.5194/acp-21-635-2021, 2021.